

Characterization of morphology—3D and porous structure

2

H.J. Haugen*, S. Bertoldi^{†,‡}

*Department of Biomaterials, Institute of Clinical Dentistry, University of Oslo, Oslo, Norway, [†]Department of Chemistry, Materials and Chemical Engineering “G. Natta”, Politecnico di Milano, Milan, Italy, [‡]INSTM Local Unit Politecnico di Milano, Milan, Italy

2.1 3D porous structures: porosity and other relevant morphological parameters

Three-dimensional (3D) porous structures find applications in the biomedical field mainly as scaffolds for tissue engineering and regenerative medicine, as for most tissues (e. g., bone tissue, blood vessel, muscle tissue) a porous support guiding growing tissue is crucial. Their characterization appears to be fundamental, as the architectural parameters, porosity in particular, but also pore size and interconnectivity [1,2], strongly affect the mechanical and biological performance of the 3D structures [2,3], and thus their functionality.

Effective techniques, able to provide information on scaffold morphological properties, are required at the initial stages of research and development, so to design scaffolds with the optimal properties for the specific application. In addition, since the biological performance of the scaffolds should be evaluated with respect to their ability during time to favor cell adhesion, proliferation, and extracellular matrix production, an analytical technique capable of monitoring the evolving steps of a cell/tissue-biomaterial interaction experiment, both *in vitro* and *in vivo*, can be very useful. The need for measurements and standard rules to be applied for scaffold characterization is well identified by scientists and regulators [4], and the debate about that is vivid.

Among the morphological parameters to be analyzed (Table 2.1), porosity is the most often quoted [5], as it would influence scaffold mechanical properties and scaffold-cell interactions. Considering the description reported in Table 2.1, porosity does not provide any clue regarding how pores are distributed through the sample.

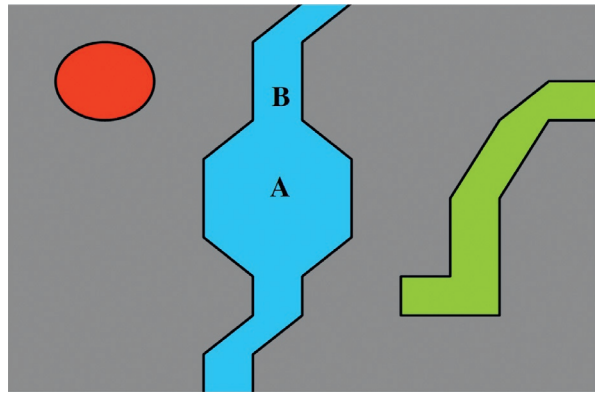
Porous materials can present three different pore types [2,3,5], as schematically shown in Fig. 2.1: enclosed pores isolated within a matrix (red), open pores or through pores connecting the outer surface of the scaffold (blue), and blind-end pores in contact with an exposed internal or external surface through a single orifice (green).

All these kinds of pores play a role in biomedical applications of 3D structures. In particular, through pores are essential for scaffold function, i.e., mechanical and structural support of the newly forming tissue, and are correlated to another fundamental property, that is, pore interconnection (Table 2.1). Besides porosity and interconnectivity, also pore size, defined as the average pore diameter, is a key micro-architectural

Table 2.1 Main morphological features to be analyzed for scaffold characterization

Property	Description
Porosity	Ratio between the total pore volume (V_i) and the sum of pore volume and scaffold material volume ($V_i + V_s$)
Pore size	Average pore diameter
Wall size	Average size of the wall/strut separating the pore
Interconnection	Ratio between the volume of the interconnected pores (V_i) and the sum of interconnected porosity and closed porosity ($V_i + V_c$)
Anisotropy	Not homogeneous orientation of the scaffold struts and pores

Fig. 2.1 Schematic representation of the different pore types that can exist within a scaffold: closed pores (red), open pores (blue), and blind-end pores (green) A indicates pore cavity and B indicates pore throat [2].



parameter to be considered and controlled, as it can influence cell attachment and penetration.

Several techniques for the assessment of scaffold morphological properties have been proposed, including microscopy observation, mercury porosimetry, gas pycnometry, and capillary flow porometry. A recently published review [3] provides information about all cited techniques. It is here worth noticing that a single technique is often limited and suitable only for the assessment of a specific parameter, and each of these techniques has several drawbacks. For these reasons, a combination of different techniques is often required so to achieve an in-depth study of the morphologic properties of the scaffold. Table 2.2 presents in a schematic way each technique, specifying achievable parameters, advantages and disadvantages.

2.2 Morphological characterization by microscopy observation

Image analysis based on microscopy observation is one of the most popular approach to study the structure of 3D porous structures and scaffolds for tissue engineering, and for obtaining quantifiable data on pore sizes and the overall level of porosity,

Table 2.2 Achievable information, advantages and disadvantages of some important techniques that can be used for the characterization of 3D porous structures

Technique	Achievable morphological parameters	Advantages	Disadvantages
Microscopy observation (optical microscope, SEM and TEM)	Qualitative assessment of morphology, strut and pore size, pore interconnection, cross-sectional area, and anisotropy	Simple, not expensive and not time-consuming technique; low or very low preparation of the sample (except for TEM)	Quantitative data achievable only by the use of image analysis software; concerns in focusing materials with low opacity (i.e., polymers), artifacts, and edge effects due to scaffold preparation (for SEM and TEM)
Gas pycnometry	Open porosity	Technique usable to almost all the materials, preparation of the sample is not needed	Only open porosity can be achieved; technique sensitive to change in room pressure and temperature
Mercury porosimetry	Open porosity, pore size, and pore size distribution	Able to quantify different morphological parameters	Safe risks related to the use of mercury, destructive technique, high pressure applied can lead to artifacts in measures
Flow porosimetry	Minimum, maximum, and mean pore size	Almost user friendly technique, mainly used for the analysis of filtration membranes	closed and blind pores cannot be analyzed

being a simple, not expensive, and not time-consuming technique. The ASTM Standard Guide for Interpreting Images of Polymeric Tissue Scaffolds F2603-06 [6] provides fundamental factors that have to be considered in obtaining and interpreting images of tissue scaffolds, including selection of the best microscopy technique according to the material to be analyzed, instrument resolution and image quality, quantification, and sample preparation.

Optical microscope can be used to obtain images of the surfaces of tissue scaffolds. The main advantage of this technique is the minimal specimen preparation needed, but its use is strongly limited by the low opacity of most of the materials used for scaffold fabrication and by the difficulties in focusing 3D porous structures [7].

Both Transmission Electron Microscopy (TEM) and Scanning Electron Microscopy (SEM) can be used to image sectioned scaffold surfaces or sections, interpreting the images by the use of image analysis software packages to generate data concerning the shape of pores within the scaffold, their mean size, and distribution [8,9]. In addition, SEM enables a visual estimation of interconnectivity, cross-section area, and anisotropy of the pores. The estimation of both permeability and tortuosity can be made from 3D virtual images generated from TEM images of serially sectioned samples [7].

As previously mentioned, both optical microscope and SEM are used for the morphological characterization of porous scaffolds in almost all the research papers present in the scientific literature. A very interesting approach is proposed by Guarino et al. in [10]. According to ASTM F2603-06 Standard Guide [6], the Authors developed a method for SEM image processing, to provide general shape metrics to compare results of an edge-based algorithm for segmentation, implemented on poly- ϵ -caprolactone porous scaffolds by a self-implemented MATLAB code, with the computer-aided manual segmentation provided by the software ImageJ. By this method, they were able to calculate also pore interconnection degree. The values of porosity percentage and average pore size obtained by this method resulted in strong agreement with the values experimentally obtained by mercury intrusion porosimetry (cfr. 2.5).

On the contrary, TEM is not so often applied in 3D structure characterization, requiring more efforts in scaffold preparation and being more time consuming. For this reason, some literature examples about the use of TEM in 3D porous structure characterization are here reported. In a recent paper [11] Sadeghzade et al. assessed the morphological properties of baghdadite nanostructured scaffolds for bone tissue engineering by use of SEM and TEM. In particular, SEM was used to investigate the pore morphology and analyze the scaffold surface, while TEM, thanks to the very high magnification that can be reached, was useful to evaluate the grain size and the morphology of powder used to produce the scaffolds. TEM can be successfully used also to morphologically characterize 3D porous nanocomposites, in particular to evaluate the dispersion of the nano-sized loading in the matrix, as performed by Pal et al. [12]. Furthermore, TEM is extremely effective in assessing the morphology of nanofibrous polymeric scaffolds and matrices, analyzing in particular the dimension and morphology of the fibers [13,14]. Castillo-Ortega et al. [14] were able to observe the structure of cellulose acetate-poly(vinyl pyrrolidone) fibrous membrane obtained by electrospinning before and after the release of epicatechin (Fig. 2.2).

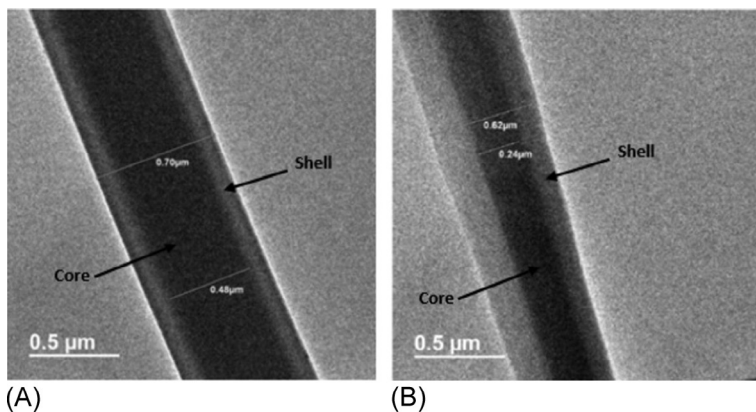


Fig. 2.2 TEM micrographs of a cellulose acetate-poly(vinyl pyrrolidone) electrospun fiber before (A) and after (B) epicatechin release. Fiber dimensions are measured, indicating core and shell of the fiber. Scale bar = 0.5 μm [14].

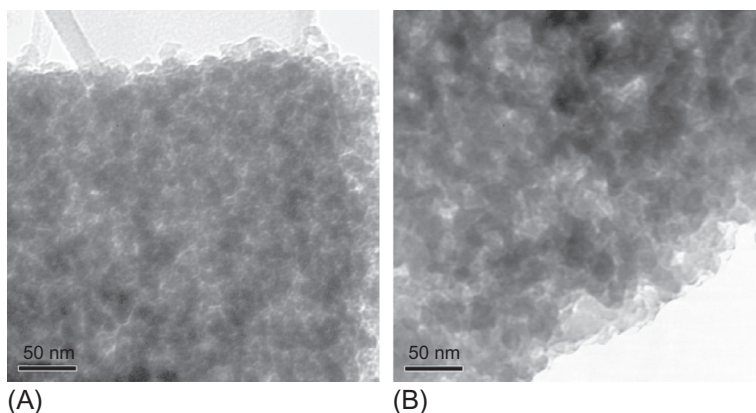


Fig. 2.3 Bright field TEM micrographs of a bioactive glass specimen near the surface (A) and at the center of the sample (B). Scale bar = 50 nm [15].

At the same way, the nanopore network of 3D nano-macro porous bioactive glass scaffolds can be very well visualized and analyzed by use of TEM (Fig. 2.3) [15].

There is a high degree of uncertainty in the reliability of quantitative data derived from electron microscopy examination of soft or highly hydrated soft polymer-based scaffolds, due to the presence of artifacts and edge effects created during sample scanning and observation. These problems may be overcome by using environmental SEM, as it is possible to analyze the sample not under vacuum, thus reducing the possibility to distort soft polymer scaffolds. In addition, microscopy observation techniques consider very small area of the specimen (i.e., 500 μm × 500 μm) that cannot be representative of the whole scaffold.

Therefore while SEM or other microscopic techniques provide a sharp and realistic view of the 3D scaffold structure with large depth of field, the important pore architectural features of the scaffolds, such as porosity, pore and strut size distribution, and interconnectivity of the 3D pore space cannot be fully quantified, as the observation is related only to a specific area of the specimen and it does not take into account the 3D structure of the material. Therefore, in general, these image-based techniques are used for a preliminary assessment of the scaffold morphology and to qualitatively estimate pore shape, size, and distribution.

2.3 Determination of porosity by density measurements

Density measurements and theoretical methods are often used, combined with SEM observation, to characterize scaffold morphology, but they are useful only to evaluate the porosity of the 3D structure.

An estimation of the scaffold pore volume can be obtained using the relationship between density and volume, providing that the density of the bulk material, ρ_M , used to produce the scaffold is known. The mass of the sample, m_S , can be easily measured to a high level of accuracy, and for hygroscopic materials after drying the sample to constant weight to avoid any measured artifact due to humidity. The volume V_T of the sample is determined by measuring the sample dimensions. However, this measurement could be particularly difficult when measuring the volume of a sample with irregular shape or made by a very soft material. In fact, soft structure can be flattened when measuring their dimensions by the use of a caliper. Irregular shape can instead cause problems in obtaining a precise and average linear dimension.

The volume of pores within the samples, V_P , is then calculated according to Eq. (2.1):

$$V_P = V_T - \frac{m_S}{\rho_M} \quad (2.1)$$

and the percentage porosity is $V_P/V_T \times 100$.

Some of the issues arising by the use of density measurements can be overcome by applying the Archimedes Principle (i.e., buoyancy method) [2,5,16], which states that the volume of liquid displaced by an object completely immersed in it is equal to the volume of the object. In this method (Fig. 2.4), the dry weight W_{DRY} of the sample is measured. Then the specimen is put in a liquid, for example, water, under negative pressure to allow the complete penetration of the water within the structure and the submerged weight W_{SUB} is recorded. The specimen is removed from water and its wet mass W_{WET} is measured. The apparent porosity value, i.e., the ratio of total volume of open pores in a porous body to its bulk volume can be obtained by Eq. (2.2):

$$\text{Porosity} = \frac{W_{WET} - W_{DRY}}{W_{WET} - W_{SUB}} \quad (2.2)$$

The main drawback of the Archimedes method is that it is not appropriate for hydrophobic materials, as water could not penetrate into the pores because of the lack of

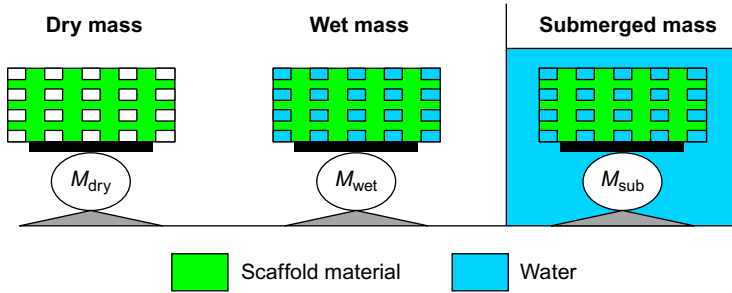


Fig. 2.4 Archimedes method to evaluate structure porosity [2].

affinity between the water and the hydrophobic surface. For moderately hydrophobic materials the consistency of repeated measurements can be significantly improved by exposing the sample to an extended period of soaking and agitation until W_{SUB} becomes stable [5]. Furthermore, in hydrophilic polymeric structures water can induce shrinkage or swelling, thus creating artifacts.

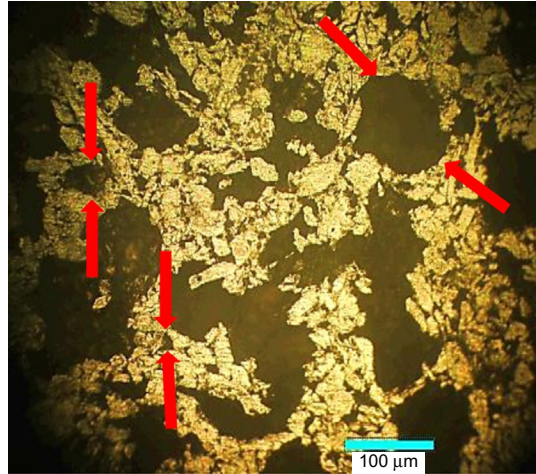
The density-based method for porosity evaluation allows estimating the total free space (i.e., volume of open pores, blind-end pores, and closed cells) of a specimen/scaffold. This value could be useful, but it has limited practical relevance, since it does not take into account the different types of pores composing the whole porosity, and therefore they are relevant only for 3D structure in which the proportion of enclosed or blind-end pores is negligible.

Density-based methods are quite often applied in research works to assess the porosity of 3D structures. For example, Chen et al. [17] evaluated the porosity of electrospun polyurethane-collagen mats by calculating the mats' apparent density (as ratio between mats mass and mats volume) and dividing it by the material bulk density. Obtaining a precise measure of the mat linear dimensions (needed to calculate the mat volume) is very difficult, and this inaccuracy can lead to a not reliable value of porosity. The authors highlighted also the difficult quantification of the bulk density of the material [17]. Vitale-Brovarone et al. [18] used the same method described earlier to calculate the porosity of 3D porous glass-ceramic scaffolds for bone tissue regeneration. They did not report any difficulty in measuring sample linear dimensions, as the scaffolds they developed were rigid and with regular shape.

Kalantari et al. [19] applied the Archimedes principles, combined with the software Image Tool, to quantify the porosity of scaffolds made of titanium alloy (i.e., Ti-6Al-4V), loaded with magnesium (Mg) powder. They verified the increase in scaffold porosity by increasing the Mg content (from $47\% \pm 6\%$ without Mg to $64\% \pm 10\%$ for samples containing 60% volume of Mg) and the presence of micro and macro pores within the scaffold structure (Fig. 2.5).

Yang et al. [20] developed a modified Archimedes method to evaluate the porosity of poly(L-lactic acid) and poly(L-lactic-co-glycolic acid) scaffolds. In particular, ethanol, instead of water, was used as displacement liquid. A density bottle filled with ethanol was weighed (W_1). A scaffold sample of weight W_S was immersed into the

Fig. 2.5 Micro and macro pores in the scaffold morphology. Scale bar = 100 μm [19].



density bottle, and the air bubbles in the scaffold pores were eliminated under vacuum, so to allow the penetration of the ethanol within the pores. Then the density bottle was fully filled with ethanol and weighed (W_2). The scaffold saturated with ethanol was taken out of the density bottle and then the density bottle was weighed (W_3). The porosity was then calculated according to the formula (2.3):

$$\text{Porosity} = \frac{W_2 - W_3 - W_s}{W_1 - W_3} \quad (2.3)$$

They were able to demonstrate that porosity increases with the porogen weight fraction, obtaining a good correspondence between the porosity and the weight fraction values.

2.4 Gas pycnometry

A gas pycnometer can be used for measuring the density or more accurately the volume of solids using method of gas displacement, by applying the pressure relationship known as Boyle's law. A gas pycnometer is also sometimes referred to as a helium pycnometer [21].

While pycnometers are recognized as density measuring devices, these devices merely measure volume. Density is simply calculated as the ratio of mass to volume, mass being invariably measured on a discrete device, usually by weighing [22]. The volume measured in a gas pycnometer is that amount of 3D space which is inaccessible to the gas used, i.e., that volume within the sample chamber from which the gas is excluded. Therefore the volume measured considering the finest scale of surface roughness will depend on the atomic or molecular size of the gas. Helium therefore is most often prescribed as the measurement gas, as it is inert and composed by molecules of small size, and therefore the most ideal gas [21].

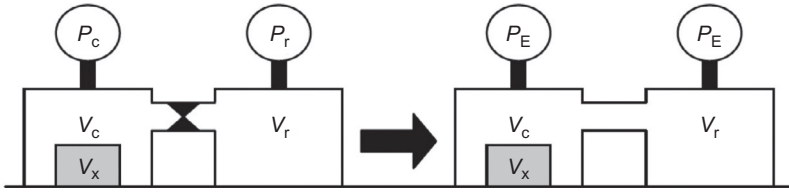


Fig. 2.6 Schematic representation of gas pycnometry equipment for porosity evaluation [2].

By the use of a gas pycnometer, the porosity can be assessed by detecting the pressure change due to the displacement of the gas by the material (Fig. 2.6).

The porosity of a sample is calculated by a simple equation (Eq. 2.4) from the open pore structure divided by the solid body:

$$\text{Porosity} = \frac{V_g - V_i}{V_g} \times 100 \quad (2.4)$$

where V_g is the geometrical volume, i.e., the volume of the specimen determined by measuring its geometrical dimensions, and V_i is the impenetrable volume, that is the volume of the test specimen into which gas cannot penetrate, under the test conditions.

The main drawback with this technique is that it cannot differentiate between open and closed pores. In fact, the closed pores cannot be penetrated by gas, and so the volume of the closed pores is included in the impenetrable volume V_i , together with the volume of the closed pores is included in the impenetrable volume V_i , together with the volume of the material (solid volume). Additionally, helium may however demonstrate some measurable permeability through low density solids (polymers and cellulosic materials predominantly) thus interfering with the measurement of solid volume. In fact in this case also the solid volume, i.e., the volume of the material itself, would result to be penetrable to the gas, even if it has to be encountered in the impenetrable volume V_i . In such cases the use of larger molecule gases, such as nitrogen, is beneficial [23]. Adsorption of the measuring gas should be avoided, as should excessive vapor pressure from moisture or other liquids present in the otherwise solid sample. For these reasons, the sample should be pretreated in a vacuum oven to remove volatiles that can interfere with the measured gas. The contribution of the instrument to measure inaccuracy is, for the most part, confined to leaks and temperature instability or temperature gradients. The measure obtained by gas pycnometer is, in fact, based on the displacement of the gas that is related to a change pressure according to the Boyle's law. The Boyle's law requires performing the measurements at fixed and constant temperature, so the room temperature should be set and monitored during the analysis. Another source of error that has to be taken into account relies in the difficulty in taking accurate linear dimensions (i.e., the dimensions used to calculate the volume) of the specimen to be tested so to calculate the volume of the specimen, in particular when working with flexible materials.

The gas pycnometry method was quite often used in the early 2000s to evaluate scaffold porosity [24,25]. More recently, Enrione et al. [26] measured the porosity of gelatin/chitosan/hyaluronic acid scaffolds by use of a gas pycnometer with helium

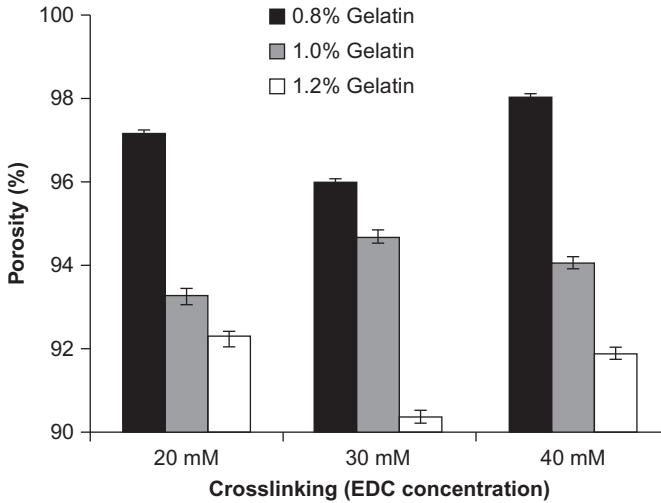


Fig. 2.7 Porosity of the different scaffold formulations obtained by varying gelatin and crosslinking agent concentration [26].

as displacement gas, and they were able to assess the influence of the scaffold composition on the morphological properties, in particular on porosity (Fig. 2.7).

Helium pycnometer can be used also to evaluate the bulk volume of porous acrylic matrices loaded with ibuprofen, as performed in [27].

2.5 Mercury porosimetry

Porosimetry is an analytical technique used to determine material's pore structure, in particular pore size and pore size distribution, by intrusion of a liquid. Mercury, a non-wetting liquid, is intruded into the porous structure with increasing pressure. The pore size can be calculated by Washburn's equation:

$$D = \frac{-4\gamma \cos \theta}{P} \quad (2.5)$$

where D is the pore diameter, γ is the surface tension of mercury, θ is the contact angle of mercury, and P is the differential gas pressure. Using the Washburn equation, pore sizes and pore volume distribution by pore size are calculated [28].

Fig. 2.8 helps to explain the technique of mercury porosimetry. The sample is placed inside the intrusion chamber that has to be evacuated to remove contaminant gases and vapors. The intrusion chamber is filled with mercury until a maximum pressure, at which time the total intrusion volume reached a plateau. This creates an environment consisting of a solid (the sample), a nonwetting liquid (mercury), and mercury vapor. Pressure is increased toward ambient pressure, so to allow the derivation of apparent scaffold volume, while the volume of mercury entering larger pores is monitored.

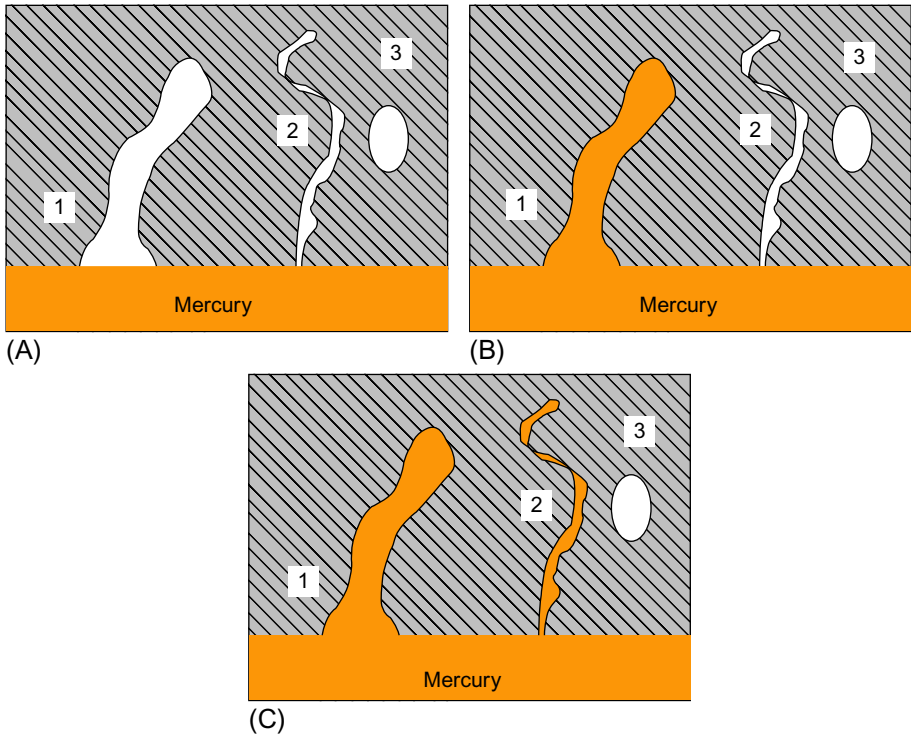


Fig. 2.8 Mercury porosimetry technique for pore size evaluation. At ambient pressure, the sample is enveloped by mercury (A). As mercury pressure increases, the large pores (1) are filled with mercury first (B). Pore sizes and pore volume distribution by pore size are calculated as the mercury pressure increases. At higher pressures (C), mercury intrudes into the fine pores (2) and when the pressure reaches a maximum, total open pore volume and porosity are calculated. The closed pores (3) are neglected in this assay as they are not intruded with mercury [2].

Maximum pressure is attained by means of incremental steps to promote mercury intrusion. At maximum pressure, the total volume of the intruded mercury is measured, enabling the derivation of total open pore volume and porosity [2,3].

This technique is excellent for measuring materials characterized by small pore sizes and low porosity, such as ceramics.

Important information on material's physical and morphological properties (e.g., pore tortuosity, sample compressibility, permeability, density, pore cavity-to-pore throat ratio, and pore cavity size distribution) can be obtained analyzing the intrusion and extrusion curves, obtained by plotting the cumulative volumes of mercury, respectively, when intruding and extruding the mercury varying the applied pressure. According to the shape of the pores, the extrusion curve usually does not follow the same plotted path as the intrusion curve. Therefore the intrusion and extrusion curves contain different information about the pore network. Hysteresis in intrusion and

extrusion curves is attributable to pore shape. Hysteresis loops of various shapes often are observed and many do not close when pressure is reduced; this can be attributed to large cavities being interconnected by smaller pore throats. In fact, although large pores fill at low pressures, a large cavity connected to the surface by a small throat cannot fill until the pressure is sufficient to fill the smaller connecting throat. Upon decompression, the small throat empties at the same pressure at which it is filled, but the large cavity behind the throat remains filled. The pore will empty at the lower pressure associated with its radius or it may not empty at all if the path to the surface is composed of pores of too different sizes. So, intrusion of mercury into a cavity is controlled by the size of the pore throat radius while the radius of the cavity and its connectivity controls extrusion of mercury from the cavity. Applying these considerations, pore cavity-to-pore throat ratio and the distribution of pore cavity sizes associated with pore throat sizes can be calculated [29].

Another parameter that can be obtained by intrusion and extrusion curves is permeability, that is, the inherent ability of a porous material to transmit a fluid and is a property of the material itself. Permeability is related to porosity as it can be considered the “proportionality constant” linking fluid flow rate to applied pressure across a porous material. There have been many attempts to relate permeability to some relevant microstructural parameters, and the work of Katz and Thompson provides an important contribution to mass transport studies in facilitating the prediction of fluid permeability of materials from mercury injection data [30,31].

However, this technique does not inform the user about porous structure’s interconnectivity, strut/wall thickness, anisotropy, and cross-sectional area, nor closed pores, as mercury does not intrude into closed pores. Other drawback is that the samples need to be discharged afterward since mercury is toxic and therefore the technique destructive. The penetrometers, in which the samples are placed, are made of glass and have a brittle nature, and therefore they need to be handled carefully to avoid mercury spillage [32].

Despite some drawbacks, mercury porosimetry is widely used for the assessment of scaffolds’ morphological properties. Table 2.3 summarizes some research works in which mercury intrusion porosimetry was applied to evaluate porous structures’ porosity.

As reported in Table 2.3, mercury intrusion porosimetry was used for characterization of several types of scaffold, produced with very different materials and therefore characterized by completely different physical and mechanical properties. Not always this method can be applied without introducing artifacts and errors affecting the obtained results. Particular attention has to be paid when analyzing scaffolds made by very soft materials (i.e., natural polymers) or with low thickness (i.e., electrospun mats and scaffolds). Furthermore, several authors [39–41] report misestimation of porosity and pore size, mainly due to the technique limits highlighted as follows (e.g., high pressure that can break the pore walls, limits in analyzing pore with dimensions higher than 250 μm , hypothesis of cylindrical pore shape). An incoherence between micro-CT results and mercury porosimetry data can be detected both in pore size (Fig. 2.9A) and in void fraction percentage (Fig. 2.9B). In both cases, mercury porosimetry seems to overestimate the morphological parameters.

Table 2.3 Scientific papers describing mercury porosimetry to characterize the scaffold porosity

Materials and type of structure	Morphological parameters analyzed	Main results	Reference
Poly- ϵ -caprolactone porous scaffolds obtained by thermally induced phase separation and salt leaching technique	Porosity and average pore size	Results in strong agreement with SEM image processing and analysis	[10]
Collagen crosslinked with 2,3-dialdehyde cellulose foams obtained by freeze-drying	Porosity, pore size, pore size distribution, and surface area-to-pore volume ratio	Crosslinking causes a significant decrease in pore size; values of pore size comparable to the ones obtained by SEM observation and image software analysis	[33]
Poly(L-lactide-co- ϵ -caprolactone) scaffolds obtained by thermally induced phase separation	Porosity, pore size, and pore size distribution	Congruence between results obtained by mercury porosimetry and SEM images	[34]
Chitosan/hydroxyapatite porous composites obtained by freeze-gelation	Porosity, pore size, and pore size distribution	Not complete coherence between results of mercury porosimetry and SEM images, probably because of the not correct hypothesis of material having cylindrical pores	[35]
Porous magnesium/poly-lactide-co-glycolic acid composites obtained by solvent casting/particulate leaching	Pore size and pore size distribution	Pore size not comparable with the dimension of sodium chloride crystals used for particulate leaching	[36]
Hydroxyapatite/proteins composites obtained by freeze-drying	Porosity and pore size distribution of pores in the range 5 nm to 1 μ m	Authors highlighted an instrument limitation in analyzing pores larger than 1 μ m	[37]
Electrospun scaffolds made of poly(3-hydroxybutyrate)/gelatin/nanohydroxyapatite	Porosity, pore size, and pore size distribution	Good porosity values and very low values of pore size, not in agreement with SEM images	[38]

Continued

Table 2.3 Continued

Materials and type of structure	Morphological parameters analyzed	Main results	Reference
Scaffolds prepared by salt leaching of a photopolymerized dimethacrylate	Porosity, pore size, and pore size distribution	Mercury porosimetry underestimated porosity and overestimated average pore size if compared to micro-CT and gravimetric analysis results	[39]
Polyurethane foams obtained by thermally induced phase separation with a subsequent freeze-drying step	Pore size distribution	Mercury porosimetry underestimated pore volume if compared to SEM observation and image analysis	[40]
Crosslinked poly(propylene fumarate) scaffolds obtained by solvent casting/particulate leaching	Porosity	Mercury porosimetry overestimated porosity if compared to micro-CT results	[41]

Information about scaffold material, morphological parameters achieved, and remarkable results are reported.

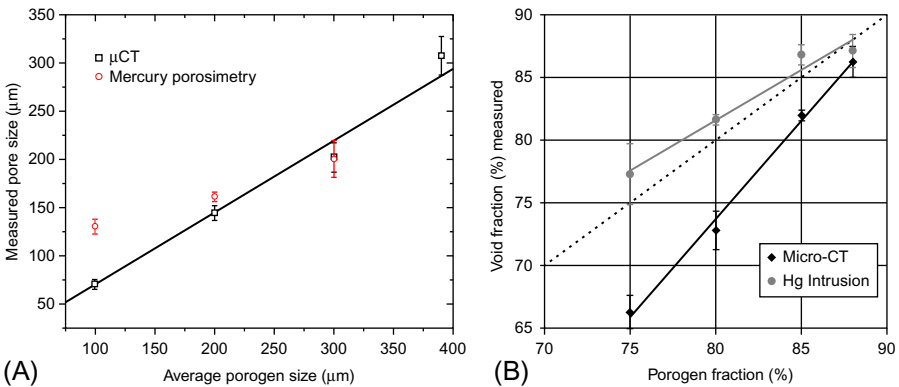


Fig. 2.9 Comparison of the average pore sizes obtained from micro-CT and from mercury porosimetry of photopolymerized dimethacrylate scaffolds prepared by salt leaching. The line represents a linear fit of the micro-CT data (A). Reprinted with permission from Lin-Gibson S, Cooper JA, Landis FA, Cicerone MT. Systematic investigation of porogen size and content on scaffold morphometric parameters and properties. *Biomacromolecules* 2007;8(5):1511–8. Copyright 2017 American Chemical Society; mean void fractions of poly(propylene fumarate) scaffolds obtained by solvent casting/particulate leaching with four different porogen contents, as measured with micro-CT and mercury porosimetry. Solid lines represent linear regression; the broken line represents identity (1:1) [41] (B).

2.6 Flow porosimetry

A technique that is the opposite from mercury intrusion porosimeter is the capillary flow porosimetry. Opposed to mercury intrusion porosimeter, the wetting liquid is allowed to spontaneously fill all the accessible pores. A nonreactive gas under increasing pressure is then used to displace this fluid from the sample. The amount of pressure required for this process depends on the size and on the size distribution of pores. The wetting fluid is chosen such that its surface free energy with the sample is less than that of the sample with the gas. This enables the gas to displace the wetting fluid, replacing the liquid-sample interface by a high free energy gas-sample interface. The pressure required to empty the pore corresponds to the pressure necessary to evacuate the liquid from the most constricted part of the pore (i.e., bottle-neck). The gas pressure and flow rates through wet and dry samples are accurately measured. The gas pressure required to remove liquid from the pores and cause gas to flow is given by the same equation as for mercury intrusion porosimeter (Eq. 2.5). The most constricted part of the pore is the most challenging one and it offers the highest resistance to remove the wetting liquid. This measured pressure permits to obtain the pore diameter, which is calculated by using the Young-Laplace formula (Eq. 2.6):

$$P = \frac{4\gamma \cos \theta}{D} \quad (2.6)$$

in which D is the pore size diameter, P is the pressure measured, γ is the surface tension of the wetting liquid, and θ is the contact angle between the wetting liquid and the sample. The surface tension γ is a measurable physical property and depends on the wetting liquid used. The contact angle θ depends on the interaction between the material and the wetting liquid.

Use of low surface tension wetting liquid simplifies the equation considerably because the contact angle of low surface tension liquids is close to zero [42]. So, for low surface tension liquids, Eq. (2.6) reduces to the following:

$$P = \frac{4\gamma}{D}$$

Practically, the pressure and gas flow rates through wet (i.e., filled with liquid) and dry samples are determined to give “wet” and “dry” curves. The gas flow rates through a wet sample are zero at low differential pressures, because all the pores are filled with the wetting liquid. At high pressures gas removes the liquid from pores and flows through empty pores. With increasing gas pressure, smaller pores become empty and the gas flow rate increases. At sufficiently high pressure, all the pores become empty and the flow through the wet sample becomes identical with the flow through the dry sample in which all the pores are empty. Pressures needed for gas flow through the wet sample (i.e., the wet curve) are used to compute the pore size, as the pore diameter is related to the pressure required to remove the liquid by Eq. (2.4). The flow through the dry sample is used to compute the mean flow pore size, the smallest pore,

and the gas permeability. The gas flow rates through wet and dry samples are used to compute pore size distribution. A measure of the permeability of the 3D porous structure can be obtained by monitoring the flow of air through the sample as a function of the applied pressure gradient. According to Darcy's law, the rate, Q , at which air flows through a sample of thickness L and cross-sectional area A for a range of differential pressures, ΔP , provides a measure of permeability, k (Eq. 2.7).

$$k = \frac{QL}{A\Delta P} \quad (2.7)$$

This technique is used to measure minimum, maximum (or first bubble point), and mean flow pore sizes, and pore size distribution of the through pores in polymeric and ceramic membranes [21], nonwovens, paper, filtration and ultrafiltration media, and hollow fibers [22]. These parameters are very relevant in filtration and similar applications since it is important to know the smallest diameter of the through pores.

Potential biomedical applications of this technique should not be ignored even though there is only one publication describing its use in examining scaffolds. In fact, as an example, data provided by this technique provide an indication of the scaffolds' accessibility to cell migration. The measured pore size distributions highlight the minimum pore diameters. Very small bottlenecks are not conducive to cell migration and are likely to have a negative impact on solute diffusion.

The only one paper found in the scientific literature describes a slightly modified flow porosimetry method to characterize scaffold's morphological properties [40]. The authors adapted the flow porosimetry method (i.e., the bubble point technique) to characterize pore sizes and pore size distribution of polyurethane foams obtained by temperature-induced phase separation. The sample was put in a homemade analysis chamber, equipped with a photomicroscope; *n*-dodecane, a liquid that fully wets the polymer surface, was used to completely fill the pores of the scaffold and nitrogen was applied to force the liquid out of the pores (Fig. 2.10).

The results obtained were comparable to the SEM/image analysis and mercury intrusion porosimetry data, making this technique a suitable characterization method for determining the porous architecture of 3D scaffolds.

Even though flow porosimetry is a relatively user friendly technique, it is unable to determine many important scaffold properties such as porosity, interconnectivity, strut thickness, anisotropy, permeability, and cross-sectional area. Furthermore, as the gas only passes through the through pores of the scaffold, properties of these pores are measured while that of closed and blind pores are omitted.

2.7 Micro-CT

2.7.1 Basic principles of micro-CT

Medicine took great advantage first by the simple bi-dimensional (2D) radiographic imaging, and afterward through its expansion to 3D computed-assisted tomography (CT) in the early 1970s [43]. In the same way, the analysis of bone microstructure before, and then that of 3D porous structures and scaffolds for biomedical application

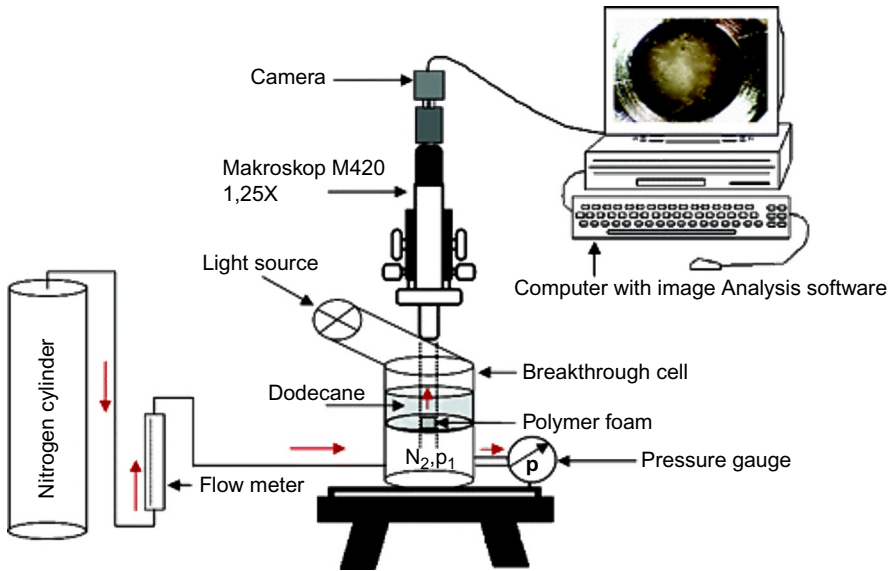


Fig. 2.10 Schematic diagram of the maximum bubble point test setup.

Reprinted with permission from Safinia L, Mantalaris A, Bismarck A. Nondestructive technique for the characterization of the pore size distribution of soft porous constructs for tissue engineering. *Langmuir* 2006;22(7):3235–42. Copyright 2017 American Chemical Society.

later, got a high improvement by the developing of micro-CT in the late 1980s. Feldkamp and his coworkers pioneered micro-CT when they developed an X-ray-based microtomographic system to analyze trabecular samples at a spatial resolution of $50\ \mu\text{m}$ [44]. While both medical CT and micro-CT share the same working statements, micro-CT was designed for smaller scaled samples and higher resolutions [43] compared to traditional CT scanners. The functioning principle is based on irradiating the studied object with an X-ray beam and recording the attenuated radiation that reaches the detector [45].

Compared to X-radiography, the main assembly difference consists in sample's rotation to a certain angle around its vertical axis, which allows for 3D rendering. In fact, micro-CT, as well as CT in general, implies taking X-ray projection images of an object from several angles around the object itself, and mathematically converting this set of images into a stack of cross-sectional image slices, which represents a 3D one. These projection images are taken incrementally over a total rotation of 180° or 360° . While the X-ray images of the individual projection are 2D, the rotation of the sample relative to the X-ray source and camera enables the precise 3D location of the scanned objects to be analyzed (Fig. 2.11) [3,46].

Two-dimensional gray-scaled virtual slices are obtained through computational algorithms, which process the signals captured at the detector. Within these projections, different levels of gray correspond to certain attenuation coefficients, while every pixel matches an exact point within the volume of the original scanned

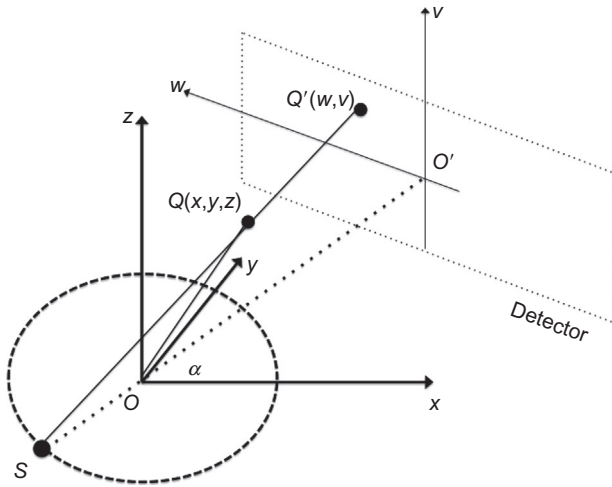


Fig. 2.11 Geometry of computed tomography. S indicates the X-ray source, O is the center of the field point of view in an x - y - z coordinate system, and O' is the center of the detector. The X-ray source and the detector have a fixed position relative to the scanned object, which rotates on a circular orbit around point O . At different angles of rotation (α), the projection images of the points O and Q (respectively, O' and Q' on the detector) have different positions. From these variable positions the absolute 3D locations of O and Q are calculated by the reconstruction algorithm.

object [2,3]. Through binarization and further analysis, information related to both void and material phases or components (e.g., different materials composing the sample or loading dispersed within a matrix), i.e., volume, interconnectivity, degree of anisotropy, density, etc., can be extracted.

Since the object is imaged in different orientations, the precise 3D location of the object structures can be calculated using computer algorithms. This process is referred to as “tomographic image reconstruction.” From these computations, a 2D pixel map is created and each pixel is denoted by a threshold value which corresponds to the material phases within the scanned sample [2]. The image resolution solves an inverse problem and essentially involves the conversion, via reconstruction algorithms, of the projection data into a 3D matrix corresponding to the tomographic representation of the specimen. The quality of the 2D maps is dependent on the scanning resolution, which can vary from 1 to 50 μm . At high resolution (i.e., 5 μm), better quality can be obtained; however, more time is required for sample scanning, data processing, and analysis.

The applicability of this characterization technique is therefore dictated by the X-ray attenuation features of the materials, which in turn depend on the atomic number of intrinsic chemical elements, material density, and sample thickness [45]. When studying metal or mineral samples no significant difficulties are faced, but some concerns may arise when working with polymers, as they are usually characterized by a low X-ray attenuation coefficient. Therefore their visualization by micro-CT can often be difficult. To overcome this problem, Crica et al. [47] proposed an approach to enhance polymer visualization by addition of high atomic number

chemicals (e.g., iodine, barium, silver-based chemicals, and hexa(methyl disilazane)) during material synthesis or postsynthesis. In particular, the most versatile methods for poly(vinyl alcohol) biopolymer composites were barium chloride additive incorporation and iodine staining coupled with hexa(methyl disilazane) chemical drying. Both methods significantly improved the X-ray absorbance of the considered polymeric samples, providing better contrast of micro-CT tomograms [47].

Micro-CT is a nondestructive technique that provides qualitative and quantitative analysis of the sample structure at high spatial resolution at micrometric scale, and it allows to determine a broad and full range of morphological parameters, such as pore shape, pore size, strut wall thickness, open and closed porosity, scaffold anisotropy, and cross-sectional area [1–3,48,49]. The interior of the specimen can be studied in great detail without resorting to physical neither sectioning nor using toxic chemicals. Moreover, after scanning, the intact samples can be subjected to other tests (e.g., mechanical characterization), therefore resolving the problem of sample scarcity. Furthermore, by measuring the total and the interconnected pore volumes, interconnectivity can be derived and the fraction of the pore volume accessible from outside through openings of a certain minimum size can be represented [22], and this is a peculiarity of the micro-CT [41].

Micro-CT has gained tremendous popularity since Feldkamp et al. [44] reported in 1989 a new method for the direct examination of 3D bone structure *in vitro*. The method combines high-resolution 3D computed tomography with algorithms that include both a generalization of conventional stereologic procedures and extensions, possible because true 3D data are available. The popularity is due to the micro-CT's ability to provide precise quantitative and qualitative information on the 3D morphology of the specimen. Feldkamp [44] reported spatial resolution of 50 μm ; however, current micro-CT systems have spatial resolution of around 2 μm . Micro-CT has applications both in medical imaging and in industrial-computed tomography. In general, there are two types of scanner setups. In one setup, the X-ray source and detector are typically stationary during the scan while the sample/animal rotates. The second setup, much more like a clinical CT scanner, is gantry based where the animal/specimen is stationary in space while the X-ray tube and detector rotate around. These scanners are typically used for small animals (*in vivo* scanners), biomedical samples, foods, microfossils, and other studies for which minute detail is desired.

One of the main drawbacks of this technique is the requiring of a thresholding (or visualization) step. In fact, the specimen to be analyzed usually consists of several discrete phases with distinct absorption or phase contrasts (as an example, for porous specimens one phase is the material and the other phase is the air within the pores). These phases occupy one or more regions within the field of view. Often, only one of these phases (e.g., the sample material, the matrix, or the loading of a composite) is of interest for computational purposes, and so the image (the volume of interest) has to be segmented into the phase of interest and everything else. Typically, the segmentation process replaces voxel values of the phase of interest by a binary value of "1" (in physical terms, these voxels are treated as solid) and the values of all other voxels with "0" (empty space). The thresholding step is performed by visual and histogrammatic estimation and is therefore user dependent and may result in inaccurate structural characterization.

2.7.2 *Micro-CT for scaffold characterization: state of the art*

The use of micro-CT in scaffold research is growing with years, even if its use in this field is still not completely exploited. In fact, there are a number of papers in the scientific literature on micro-CT analysis, but few of them are related to the use of micro-CT for the characterization of scaffolds. To date, micro-CT has been mainly used for visualizing and analyzing bone structure and development [48,50], and also for the biological study and imaging of small animals [51]. Lately, new technologies have enabled in situ examination of samples during a micro-CT scan, where one can examine material behavior under mechanical load or temperature influences.

Performing a search in Pubmed-Medline search engine, using as keywords the topics micro-CT, micro-CT+bone, micro-CT+small animal, micro-CT+scaffold, it is clear (Fig. 2.12) that just very few of the papers are related to the use of micro-CT for the morphological characterization of scaffolds.

Considering the applications of micro-CT to 3D porous structure characterization, the main topics recently discussed in the scientific community are listed as follows:

- performing a complete morphological characterization of porous scaffolds and assessing the reproducibility and suitability of different fabrication techniques for porous structure preparation with respect to the obtained morphological properties;
- monitoring during time the in vitro (and eventually in vivo) cell-material interactions and the extracellular matrix deposition;
- assessing neovascularization within the scaffolds.

2.7.2.1 *Scaffold characterization*

Performing a search in Pubmed-Medline search engine, using as keywords micro-CT+scaffold+characterization, 39 papers were recorded.

One of the advantages of the use of micro-CT emerging by the analysis of the scientific literature is the possibility to analyze structures both in dry and in wet state,

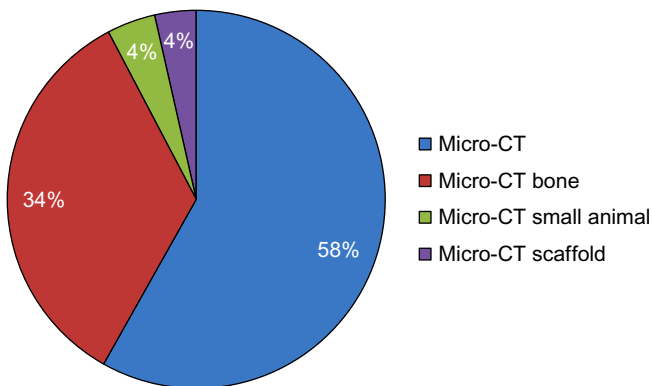


Fig. 2.12 Papers about micro-CT present in the scientific literature recorded using different keywords (research performed in Jan. 2017)

as performed in [52]. This can be particularly useful for the characterization of materials and structures with different properties in the swollen state (i.e., hydrogels). Despite this, the authors highlighted the presence of noise in the scan of the hydrated scaffolds due to the water in the structure that can introduce artifacts and has to be considered in interpreting the images and analyzing the results [52].

Micro-CT can be used also to evaluate the loading dispersion within the matrix in composite scaffolds, so to assess if the distribution is homogeneous or if the particles can aggregate in the matrix. As an example, Chen et al. [53] were able to visualize the hydroxyapatite dispersion in porous composites having as matrix a thiol-acrylate foam or a poly(ϵ -caprolactone). They generated volume renderings from composite foam 3D data using the software Avizo (i.e., a FEI Thermo-Fisher 3D analysis software for understanding materials structures and properties in a wide range of materials science research areas and for many types of materials). Two overlapping subvolumes were rendered simultaneously, one with a red-orange-white colormap corresponding to the matrix, and another with a blue-green colormap corresponding to ceramic additives. Another example of the use of micro-CT for this purpose can be found in [54], as well as in the research work of Bertoldi et al. on the characterization of polyurethane-based composites scaffolds loaded with nano-sized hydroxyapatite for bone tissue engineering (unpublished data, Fig. 2.13A and B).

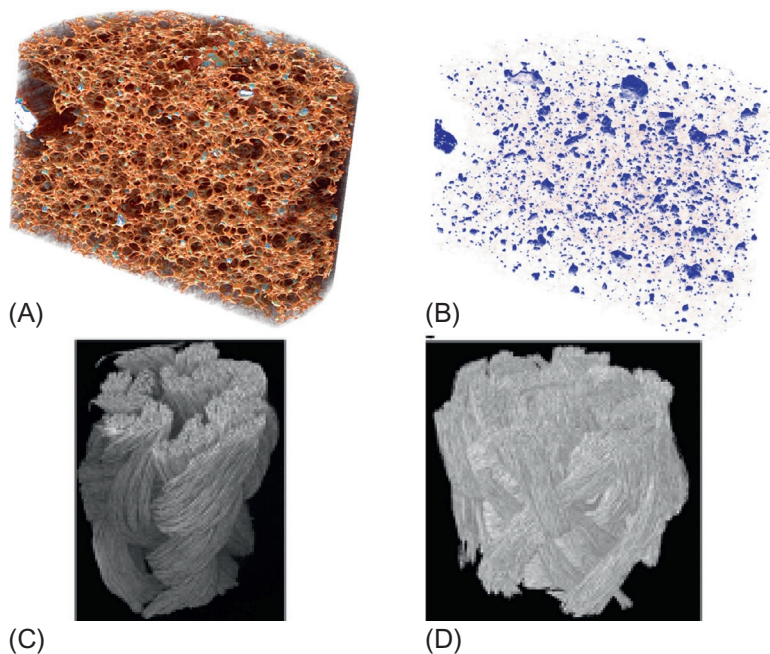


Fig. 2.13 Micro-CT 3D reconstructions of polyurethane-based composites loaded with hydroxyapatite (A), hydroxyapatite dispersion within the matrix (B) (unpublished data); micro-CT reconstruction of the core (A) and (B) the hierarchical complex structure (external sheath and internal core) [58].

Kerckhofs et al. [55] developed a nondestructive micro-CT protocol to determine the surface roughness of 3D structures. The roughness was determined based on the profile lines of the strut surfaces of the porous structures in the binarized 2D cross-sectional micro-CT images. These profile lines, extracted using an in-house developed MATLAB tool, were then used to calculate the surface roughness parameters (i.e., arithmetic mean absolute deviation of the roughness profile P_a , root mean square deviation of the roughness profile from the mean line P_q , and total height of the roughness profile P_T). They validated the proposed approach with standard roughness measurement techniques (optical and contact profilometer) and Van Bael et al. [56] applied it for the strut surface roughness of polycaprolactone scaffolds.

When fabricating multilayered composite scaffolds or structures with complex architecture, micro-CT can be a valid technique to assess the feasibility of the production process with respect to the obtained morphology. So, Koens et al. [57] verified the correct fabrication of multilayered elastin collagen tubular scaffolds by the use of high-resolution micro-computed tomographical images, and Farè et al. [58] analyzed the morphology of complex textile structures composed of a sheath and a core with different properties (Fig. 2.13C and D).

De Nardo et al. [49] exploited the micro-CT features to characterize shape memory polymer porous scaffolds obtained by solvent casting/particulate leaching, coextrusion with blowing agents or salt, gas foaming. By the results obtained by micro-CT, the authors were able to assess the suitability of the different fabrication techniques used. Furthermore, an interesting and not often considered parameter analyzed in this work is the presence of a possible preferential orientation within the material. Micro-CT allows to measure the degree of anisotropy, defining the sample structural orientation, and the fractal dimension, an indicator of the surface complexity.

An important consideration has to be done regarding the exploitation of all the potentiality of the micro-CT in scaffold characterization; in fact, only in a limited number of papers [41,49,58–60] the pore interconnection is considered and evaluated, despite this parameter is fundamental to assess scaffold functionality, and no other characterization technique is able to quantify it. Fig. 2.14 shows a possible representation of pore interconnection that can be expressed as accessible void volume as a function of connection size [60]. The interconnected pore volume decrease when increasing the diameter of the connection openings.

2.7.2.2 *In vitro cell-material interaction*

Taking advantage of the nondestructive capability of micro-CT imaging, repeated scanning can be used to monitor extracellular matrix deposition within scaffolds *in vitro*. Researchers applied micro-CT mainly to monitor mineralized matrix formation within porous scaffold both *in vitro*, as proposed in [61,62], and *in vivo* [63] (Fig. 2.15).

Assessing the bone tissue formation in calcium phosphate scaffold could be difficult, as the composition, and therefore attenuation, of the calcium phosphate and the mineral phase in bone are nearly indistinguishable. To overcome this problem Polak et al. [64] developed an algorithm, based on image automatic segmentation and filtering, to be

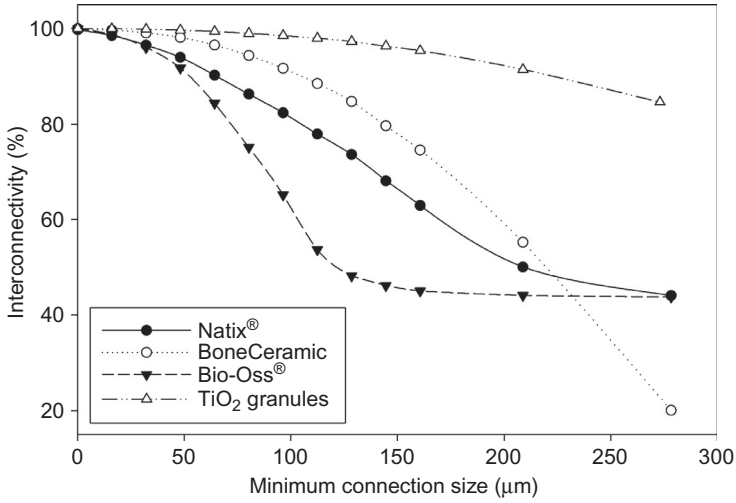


Fig. 2.14 Interconnectivity of four different bone graft substitutes through openings smaller than 280 μm in diameter. The titanium dioxide scaffolds showed better interconnectivity than BioOss and BoneCeramic. Interconnectivity allows for the migration of bone cells as well as the exchange of nutrients and metabolism products within the scaffold interior [60].

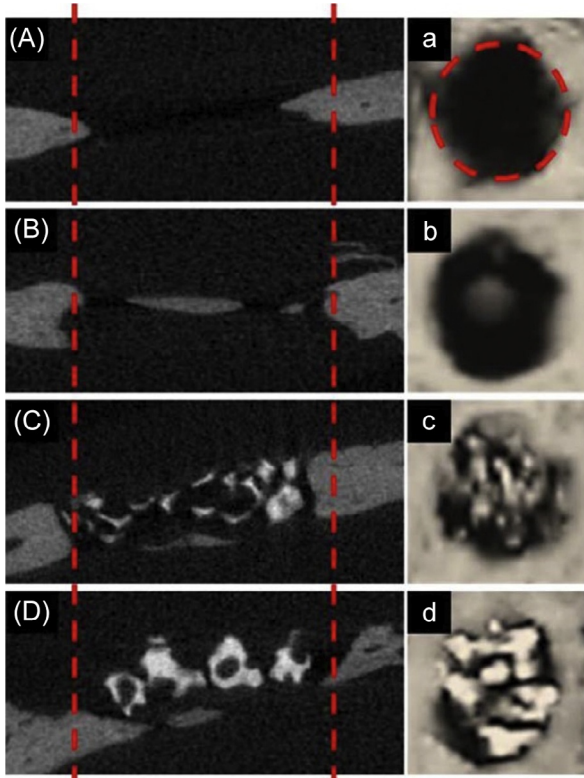


Fig. 2.15 Micro-CT images for an implanted rat calvaria defect site, after 8 weeks of implantation of blank defect as control (A), silk fibroin scaffold (B), silk fibroin-β tricalcium phosphates (particle size 300–600 μm) hybrid scaffold (C), and silk fibroin-β tricalcium phosphates (particle size 600–1000 μm) hybrid scaffold. It is evident how bone formation is enhanced in the composite scaffolds, in particular when calcium phosphates with higher particle size are used [63].

applied to micro-CT images to distinguish bone tissue and calcium phosphates composing the scaffolds. The difficulties in visualizing polymers, and therefore soft tissue extracellular matrix, still limit the use of micro-CT for the assessment of matrix formation for nonmineralized tissues. Palmer et al. [65] were able to in vitro visualize cartilage matrix with micro-CT by applying an ionic contrast agent that can electrochemically bind with the molecular charges of the cartilage matrix. The study was performed only on cartilaginous tissue, without the presence of a scaffold.

2.7.2.3 Scaffold neovascularization

Neovascularization is a critical issue in tissue engineering, and having a tool able to monitor its development over time may represent a significant benefit. Micro-CT can be useful to assess and quantify vascular ingrowth and neovascularization within 3D porous structures, combined with the use of a perfused contrast agent, needed because of the low attenuation and small diameter of blood vessels. The main advantage of the use of micro-CT for this purpose, compared to the traditionally used histologic staining assays, is that vessels form a complex network that can be better and appreciated in detail by a 3D visualization. In spite of this, because of the problem related to blood vessel visualization, there are only a few works reporting the use of micro-CT to visualize neovascularization within scaffolds [66–72]. All these papers describe the use of micro-CT to evaluate neovascularization of construct when implanted in vivo in an animal model. In particular, McFadden et al. [66] were able to demonstrate that coculturing of mesenchymal stem cells (MSCs) and endothelial cells (ECs) in collagen-glycosaminoglycan scaffolds implanted in vivo in immunocompromised rats can result in increased neovascularization (Fig. 2.16).

The beneficial use of this technique in neovascularization assessment is due to the efficacy of micro-CT analysis in quantifying morphologic parameters of 3D vessels network, including vessel volume, thickness, number, connectivity, and degree of anisotropy of a 3D vascular network.

2.7.3 Nano-CT for scaffold characterization: state of the art

As described in the previous section, micro-CT is actually widely used in 3D porous structure characterization. In some applications, the use of an instrument with a deeper resolution could allow to obtain a more detailed characterization. As an example, to assess the dispersion of a nano-sized loading within a matrix in composite structures, or to characterize nanostructured scaffolds (i.e., electrospun mats with nanosized fibers mimicking the extracellular matrix), an equipment with nano-resolution would be beneficial. Pushing this issue, technological advances permit high spatial imaging resolution and bring micro-CT into nano-CT instrument. Yin et al. reported of the construction of a microscope at the National Synchrotron Radiation Research Center (NSRRC), which can operate in the photon energy range between 8 and 11 keV and have a spatial resolution better than 60 nm in two dimensions (2D) [73]. Nano-CT has high spatial resolution spectral X-ray detection, which provides photon counts along with each photon's energy (this capability essentially duplicates imaging that was

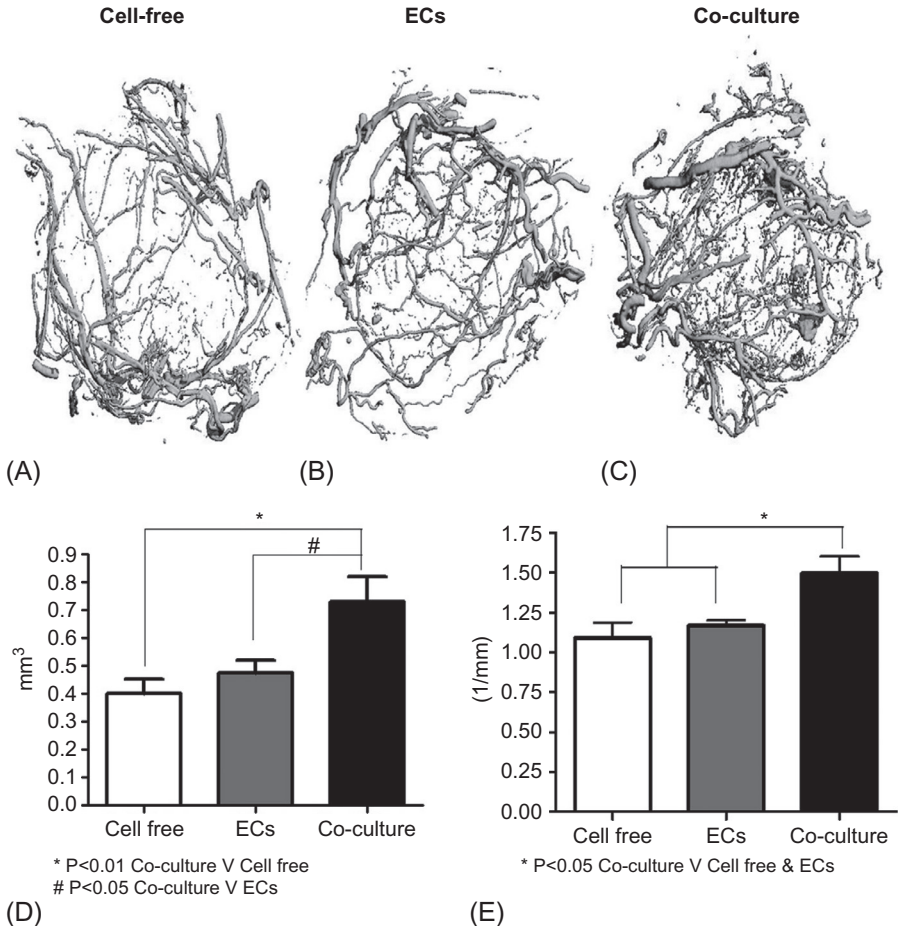


Fig. 2.16 Microcomputed tomography angiography demonstrating the level of vessel formation within the implanted constructs after 4 weeks. A reduced amount of vessel formation had occurred within the center of the cell-free scaffold (A) compared to ECs alone (B) and the co-culture group (C). The highest level of vessel formation was observed throughout the whole construct in the coculture group. Quantification demonstrated that vessel volume significantly increased in the coculture group compared to ECs alone ($P < 0.05$) and scaffold only ($P < 0.01$) (D). Vessel number was also significantly increased in the coculture group compared to the other two groups ($P < 0.05$) (E) [66].

possible only with tunable monochromatic X-ray [74,75]. Later we have seen that other synchrotron facilities have acquired the same technique [76–78]. Newer technology has enabled so-called lab-based nano-CT, which is made possible by very small X-ray focal spots and/or zone plate focusing of the X-ray beam [75]. One company claims spatial resolution down to 30 nm for such systems, whereas there are several companies that provide commercial lab-based nano-CT with resolution less than 100 nm.

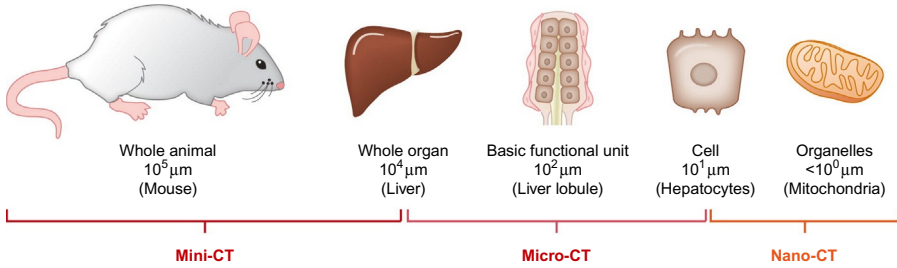


Fig. 2.17 Small rodents are of the order of 10 cm in size, their organs are 1 cm, and their tissue basic functional units (BFU) are a nominal $100 \mu\text{m}$ in diameter. Cells are of the order of 5–10 μm in diameter. The three levels of microscopic-CT can image the entire animal/organ, BFU, or cell as a single volume image, respectively [43].

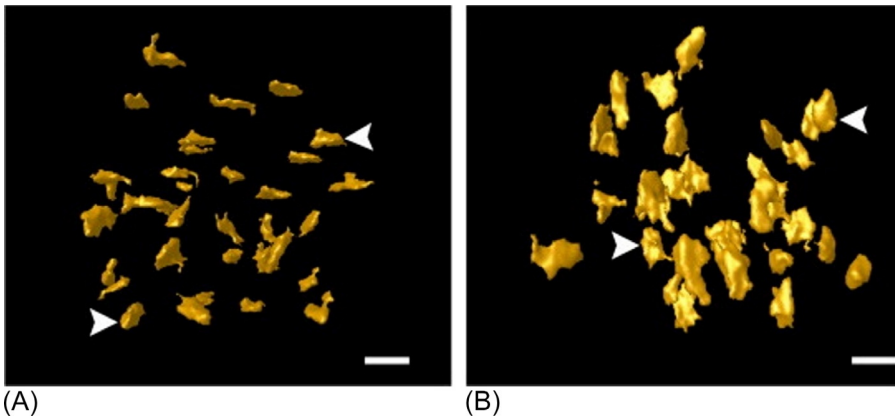


Fig. 2.18 3D reconstruction of individual osteocyte lacunae in adult mouse calvaria by using nano-computed tomography scans. (A) Longitudinal view, showing the thickness of individual lacunae (arrow heads) and showing the alignment of long axes of osteocyte lacunae in different directions, in a section of adult mouse calvaria. Bar $15 \mu\text{m}$. (B) Transverse view, showing the alignment of individual lacunae (arrow heads) in different directions. Scale bar, $15 \mu\text{m}$ [79].

The nano-CT instrument allows clear visualization of structures on the level of cells, provided that X-ray contrast is present (Fig. 2.17).

Other applications are the internal ultrastructure of bone trabeculae. For example, the internal ultrastructure of bone trabeculae, including calcification inhomogeneities and osteocyte distribution. Vatsa et al. have published a study where they use nano-CT to examine the 3D morphology of osteocyte lacunae [79] (Fig. 2.18). The high resolution of the nano-CT equipment allows to obtain a detailed and precise reconstruction of the osteocyte lacunae, and this could be exploited in the study of disease involving bone remodeling mechanism.

Phil Salmon writes in a recent book chapter that “Nano-CT occupies what was hitherto a significant gap in imaging technology, for a tomographic modality with

resolution in the range of hundreds of nanometers and sample sizes of the order of a millimetre. Due to the requirement of very small samples by nano-CT, the application of high-resolution CT imaging for the largest range of biomedical and bone research samples remains the province of ‘conventional’ desktop micro-CT scanners.” [80].

The use of nano-CT is actually very limited, in particular for 3D porous structure characterization. The main limitations of its use are the cost of the equipment and, most of all, the very long time required for the analysis that is related to the high resolution achievable.

2.7.4 Comparison of micro-CT with other techniques

Submicron structural details of a biomaterial play a major role not only for the prediction of mechanical properties but also for biodegradation rate and cells behavior [81]. Considering the example of a biomaterial, optimum porosity and material-related particularities (e.g., presence and distribution of loading or additive, surface roughness) must be established, while reproducibility is a key factor. In this regard, micro-CT represents a potent technique, which can provide exact information to support further functionality and behavior of the structures. Accurate 3D analysis and visualization of the pore structural parameters rely on applying a correct threshold on the binarized micro-CT dataset, to separate the scaffold volume from the surrounding phases. As the thresholding is typically performed by visual and histographical estimation, the threshold selection is somewhat user dependent and may result in inaccurate structural characterization. When particularly debating on low density 3D polymeric fibrous or porous (i.e., spongy or with foam-like architectures) scaffolds, high-resolution micro-CT analysis is still a great challenge to be solved. It is not only the low densities and lack of high atomic number elements that limit the contrast, but also the structural features with fibers or pore walls that are too thin to sufficiently attenuate X-ray beam and be “visible” at the detector [82]. In addition, the thresholding can result difficult when the scaffold is composed of multiple materials whose thresholding ranges overlap (i.e., composite materials composed by matrix and loading with similar attenuation coefficients), as the digital separation of these materials is a very complicated task. Besides this, as polychromatic X-ray beams are used in micro-CT, the lower energy rays would be readily attenuated by the sample resulting in a high exposure at the center of the scaffold. This effect is known as beam hardening, and as a result thresholding is no longer dependent only on radiodensity but also on specimen size [83]. Due to the low density difference within the low density materials, micro-CT characterization has been proved difficult [84,85].

Micro-CT analysis can result difficult also with metal-containing materials, as the X-rays are heavily attenuated by these materials. The presence of metals can result in dark and bright grainy artifacts which can obscure important details in the scan images.

On the one hand, scanning electron microscopy is reserved to 2D analysis, while alternative techniques such as capillary flow porometry and mercury porosimetry are as well difficult for polymeric porous materials, due to their elastic and soft structure [86,87]. Gas permeation techniques can enter the porous structure independently of

mechanical strength, however is limited to only open pores and additionally has disadvantage in large standard deviations. Thus there is a need for systematical examination on solution to enhance the resolution of low density polymeric composites in micro-CT investigations. On the other hand, choosing a suitable contrast agent is another delicate issue due to the physical-chemical nature of most biopolymers.

Nonetheless, the micro-CT scanning and subsequent image processing can be very time consuming and requires large amount of computational power, particularly if high image resolutions are desired. The efficacy of micro-CT in describing the scaffold architecture is also dependent on the capacity of the used analysis software to provide the calculation of the desired quantitative parameters, as well as on the capability of the quantification algorithms to perform accurate estimations of true material volume in the scaffold structure.

Considering the cell-material interactions, the quantitative assessment of in vivo tissue formation within a scaffold is conventionally performed ex vivo by histology on microscopic images. In this domain, compared to histomorphometry, X-ray micro-CT has shown its efficiency in providing nondestructive and rapid 3D images and model-independent measurements on bone microstructure. The use of micro-CT for the characterization of soft tissues is still often limited by the low X-ray attenuation coefficient of these tissues if compared to the bone value.

Despite the previously mentioned drawbacks of micro-CT, with respect to the other methods that can be used for morphological characterization of porous structures, it is a powerful tool, in particular being nondestructive, quite easy and fast, quite reproducible, and most of all allowing to calculate a wide range of parameters. In this last aspect relies the main advantage of micro-CT, as with a single technique a comprehensive set of data can be obtained.

2.8 Conclusions

A complete quantification of morphological features of porous materials to be applied in the biomedical field appears to be essential, both to improve scaffold design processes and to control biological and mechanical performances. Nondestructive 3D imaging techniques, such as micro-CT, are increasingly providing a powerful set of quantitative tools to aid in development and assessment of porous biomaterials. X-ray micro-CT was first used in the field of bone tissue engineering about fifteen years ago, and the number of research papers employing this technique is exponentially growing. By this, it can be extrapolated that it should become soon a standard analysis technique in the same way it has revolutionized the analysis of trabecular bone microarchitecture.

References

- [1] Lin ASP, Barrows TH, Cartmell SH, Guldborg RE. Microarchitecture and mechanical characterization of oriented porous polymer scaffolds. *Biomaterials* 2003;24(3):481–9.

- [2] Ho ST, Hutmacher DW. A comparison of micro CT with other techniques used in the characterization of scaffolds. *Biomaterials* 2006;27(8):1362–76.
- [3] Bertoldi S, Farè S, Tanzi MC. Assessment of scaffold porosity: the new route of micro-CT. *J Appl Biomater Biomech* 2011;9(3):165–75.
- [4] Simon CG, Yaszemski MJ, Ratcliffe A, Tomlins P, Luginbuehl R, Tesk JA. ASTM international workshop on standards and measurements for tissue engineering scaffolds. *J Biomed Mater Res B Appl Biomater* 2015;103(5):949–59.
- [5] Tomlins P, Grant PV, Mikhailovsky S, Mikhailovska L, James S, Vadgama P. Characterisation of polymeric tissue scaffolds. A national measurement good practice guide No. 89; September 2006, ISSN 1368-6550.
- [6] ASTM F2603-06. Standard guide for interpreting images of polymeric tissue scaffolds.
- [7] ASTM F 2450-04. Standard guide for assessing microstructure of polymeric scaffolds for use in tissue engineered medical products.
- [8] Jones JR, Atwood RC, Poologasundarampillai G, Yue S, Lee PD. Quantifying the 3D macrostructure of tissue scaffolds. *J Mater Sci Mater Med* 2009;20(2):463–71.
- [9] Jones JR, Poologasundarampillai G, Atwood RC, Bernard D, Lee PD. Non-destructive quantitative 3D analysis for the optimisation of tissue scaffolds. *Biomaterials* 2007; 28(7):1404–13.
- [10] Guarino V, Guaccio A, Netti PA, Ambrosio L. Image processing and fractal box counting: user-assisted method for multi-scale porous scaffold characterization. *J Mater Sci Mater Med* 2010;21(12):3109–18.
- [11] Sadeghzade S, Shamoradi F, Emadi R, Tavangarian F. Fabrication and characterization of baghdadite nanostructured scaffolds by space holder method. *J Mech Behav Biomed Mater* 2017;68:1–7.
- [12] Pal N, Dubey P, Gopinath P, Pal K. Combined effect of cellulose nanocrystal and reduced graphene oxide into poly-lactic acid matrix nanocomposite as a scaffold and its anti-bacterial activity. *Int J Biol Macromol* 2017;95:94–105.
- [13] Wang J, Sun B, Tian L, He X, Gao Q, Wu T, et al. Evaluation of the potential of rhTGF- β 3 encapsulated P(LLA-CL)/collagen nanofibers for tracheal cartilage regeneration using mesenchymal stems cells derived from Wharton’s jelly of human umbilical cord. *Mater Sci Eng C Mater Biolog Appl* 2017;70(Pt 1):637–45.
- [14] Castillo-Ortega MM, Montaña-Figueroa AG, Rodríguez-Félix DE, Prado-Villegas G, Pino-Ocaño KP, Valencia-Córdova MJ, et al. Preparation by coaxial electrospinning and characterization of membranes releasing (–) epicatechin as scaffold for tissue engineering. *Mater Sci Eng C Mater Biol Appl* 2015;46:184–9.
- [15] Wang S, Falk MM, Rashad A, Saad MM, Marques AC, Almeida RM, et al. Evaluation of 3D nano-macro porous bioactive glass scaffold for hard tissue engineering. *J Mater Sci Mater Med* 2011;22(5):1195–203.
- [16] Ma PX, Zhang R. Microtubular architecture of biodegradable polymer scaffolds. *J Biomed Mater Res* 2001;56(4):469–77.
- [17] Chen R, Qiu L, Ke Q, He C, Mo X. Electrospinning thermoplastic polyurethane-contained collagen nanofibers for tissue-engineering applications. *J Biomater Sci Polym Ed* 2009; 20(11):1513–36.
- [18] Vitale-Brovarone C, Vernè E, Robiglio L, Martinasso G, Canuto RA, Muzio G. Biocompatible glass-ceramic materials for bone substitution. *J Mater Sci Mater Med* 2008; 19(1):471–8.
- [19] Kalantari SM, Arabi H, Mirdamadi S, Mirsalehi SA. Biocompatibility and compressive properties of Ti-6Al-4 V scaffolds having Mg element. *J Mech Behav Biomed Mater* 2015;48:183–91.

- [20] Yang J, Shi G, Bei J, Wang S, Cao Y, Shang Q, et al. Fabrication and surface modification of macroporous poly(L-lactic acid) and poly(L-lactic-co-glycolic acid) (70/30) cell scaffolds for human skin fibroblast cell culture. *J Biomed Mater Res A* 2002;62(3): 438–46.
- [21] Polanski A, Romotows T. Pycnometer for determination of apparent and real density of porous materials. *Roczniki Chem* 1973;47:587–90.
- [22] Messow U, Bräuer P, Heuchel M, Pysz M. Test of the prediction of equilibrium diagrams in the field of liquid-phase adsorption of binary-mixtures in porous adsorbents by experimental-method. *Chem Tech (Leipzig)* 1992;44:56–9.
- [23] Tamari S, Aguilar-Chavez A. Optimum design of gas pycnometer for determining the volume of solid particles. *J Test Eval* 2005;33(2):135–8.
- [24] Zein I, Hutmacher DW, Tan KC, Teoh SH. Fused deposition modeling of novel scaffold architectures for tissue engineering applications. *Biomaterials* 2002;23:1169–85.
- [25] Lam CXF, Teoh SH, Hutmacher DW. In vitro degradation studies of customized PCL scaffolds fabricated via FDM. In: *International conference on biological and medical engineering*; 2002.
- [26] Enrione J, Díaz-Calderón P, Weinstein-Oppenheimer CR, Sánchez E, Fuentes MA, Brown DI, et al. Designing a gelatin/chitosan/hyaluronic acid biopolymer using a thermophysical approach for use in tissue engineering. *Bioprocess Biosyst Eng* 2013;36(12):1947–56.
- [27] Hasanzadeh D, Ghaffari S, Monajjemzadeh F, Al-Hallak M-K, Soltani G, Azarmi S. Thermal treating of acrylic matrices as a tool for controlling drug release. *Chem Pharm Bull* 2009;57(12):1356–62.
- [28] Abell AB, Willis KL, Lange DA. Mercury intrusion porosimetry and image analysis of cement-based materials. *J Colloid Interface Sci* 1999;211(1):39–44.
- [29] Webb P. An introduction to the physical characterization of materials by mercury intrusion porosimetry with emphasis on reduction and presentation of experimental data. *Micromeritics Instrument Corp*; 2001.
- [30] Katz AJ, Thompson AH. A quantitative prediction of permeability in porous rock. *Phys Rev B* 1986;34:8179(R).
- [31] Katz AJ, Thompson AH. Prediction of rock electrical conductivity from mercury injection measurements. *J Geophys Res* 1987;92(B1):599–607.
- [32] Diamond S. Mercury porosimetry—an inappropriate method for the measurement of pore size distributions in cement-based materials. *Cement Concrete Res* 2000;30(10): 1517–25.
- [33] Pietrucha K, Marzec E, Kudzin M. Pore structure and dielectric behaviour of the 3D collagen-DAC scaffolds designed for nerve tissue repair. *Int J Biol Macromol* 2016;92:1298–306.
- [34] Kasoju N, Kubies D, Sedlačík T, Janoušková O, Koubková J, Kumorek MM, et al. Polymer scaffolds with no skin-effect for tissue engineering applications fabricated by thermally induced phase separation. *Biomed Mater* 2016;11(1):015002.
- [35] Rogina A, Rico P, Gallego Ferrer G, Ivanković M, Ivanković H. In situ hydroxyapatite content affects the cell differentiation on porous chitosan/hydroxyapatite scaffolds. *Ann Biomed Eng* 2016;44(4):1107–19.
- [36] Brown A, Zaky S, Ray Jr. H, Sfeir C. Porous magnesium/PLGA composite scaffolds for enhanced bone regeneration following tooth extraction. *Acta Biomater* 2015;11:543–53.
- [37] Mueller B, Koch D, Lutz R, Schlegel KA, Treccani L, Rezwani K. A novel one-pot process for near-net-shape fabrication of open-porous resorbable hydroxyapatite/protein composites and in vivo assessment. *Mater Sci Eng C Mater Biol Appl* 2014;42:137–45.

- [38] Ramier J, Grande D, Boudierlique T, Stoilova O, Manolova N, Rashkov I, et al. From design of bio-based biocomposite electrospun scaffolds to osteogenic differentiation of human mesenchymal stromal cells. *J Mater Sci Mater Med* 2014;25(6):1563–75.
- [39] Lin-Gibson S, Cooper JA, Landis FA, Cicerone MT. Systematic investigation of porogen size and content on scaffold morphometric parameters and properties. *Biomacromolecules* 2007;8(5):1511–8.
- [40] Safinia L, Mantalaris A, Bismarck A. Nondestructive technique for the characterization of the pore size distribution of soft porous constructs for tissue engineering. *Langmuir* 2006;22(7):3235–42.
- [41] Moore MJ, Jabbari E, Ritman EL, Lu L, Currier BL, Windebank AJ, et al. Quantitative analysis of interconnectivity of porous biodegradable scaffolds with micro-computed tomography. *J Biomed Mater Res A* 2004;71A(2):258–67.
- [42] Gupta V, Jena AK. Advances in filtration and separation technology. *Am Filtrat Sep Soc* 1999;13B:833.
- [43] Ritman EL. Current status of developments and applications of micro-CT. *Annu Rev Biomed Eng* 2011;13:531–52.
- [44] Feldkamp LA, Goldstein SA, Parfitt AM, Jesion G, Kleerekope M. The direct examination of three dimensional bone architecture in vitro by computed tomography. *J Bone Miner Res* 1989;4(1):3–11.
- [45] Stock SR. *Microcomputed tomography: methodology and applications*. Boca Raton, FL: CRC Press; 2008.
- [46] Salmon P. *A short guide to analysis of bone by micro-CT* Skyscan N.V., Belgium.
- [47] Crica LE, Wengenroth J, Tiainen H, Ionita M, Haugen HJ. Enhanced X-ray absorption for micro-CT analysis of low density polymers. *J Biomater Sci Polym Ed* 2016;27(9): 805–23.
- [48] Peyrin F. Evaluation of bone scaffolds by micro-CT. *Osteoporos Int* 2011;22(6):2043–8.
- [49] De Nardo L, Bertoldi S, Tanzi MC, Haugen HJ, Farè S. Shape memory polymer cellular solid design for medical applications. *Smart Mater Struct* 2011;20:035004.
- [50] Guldberg RE, Duvall CL, Peister A, Oest ME, Lin AS, Palmer AW, et al. 3D imaging of tissue integration with porous biomaterials. *Biomaterials* 2008;29(28):3757–61.
- [51] Schambach SJ, Bag S, Schilling L, Groden C, Brockmann MA. Application of micro-CT in small animal imaging. *Methods* 2010;50(1):2–13.
- [52] Offeddu GS, Ashworth JC, Cameron RE, Oyen ML. Structural determinants of hydration, mechanics and fluid flow in freeze-dried collagen scaffolds. *Acta Biomater* 2016;41:193–203.
- [53] Chen C, Garber L, Smoak M, Fargason C, Scherr T, Blackburn C, et al. In vitro and in vivo characterization of pentaerythritol triacrylate-co-trimethylolpropane nanocomposite scaffolds as potential bone augments and grafts. *Tissue Eng A* 2015;21(1-2): 320–31.
- [54] Poh PS, Hutmacher DW, Stevens MM, Woodruff MA. Fabrication and in vitro characterization of bioactive glass composite scaffolds for bone regeneration. *Biofabrication* 2013;5(4):045005.
- [55] Kerckhofs G, Pyka G, Moesen M, Van Bael S, Schrooten J, Wevers M. High-resolution microfocus X-ray computed tomography for 3D surface roughness measurements of additive manufactured porous materials. *Adv Eng Mater* 2013;15(3):153–8.
- [56] Van Bael S, Desmet T, Chai YC, Pyka G, Dubrue P, Kruth JP, et al. In vitro cell-biological performance and structural characterization of selective laser sintered and plasma surface functionalized polycaprolactone scaffolds for bone regeneration. *Mater Sci Eng C Mater Biol Appl* 2013;33(6):3404–12.

- [57] Koens MJ, Faraj KA, Wismans RG, van der Vliet JA, Krasznai AG, Cuijpers VM, et al. Controlled fabrication of triple layered and molecularly defined collagen/elastin vascular grafts resembling the native blood vessel. *Acta Biomater* 2010;6(12):4666–74.
- [58] Farè S, Torricelli P, Giavaresi G, Bertoldi S, Alessandrino A, Villa T, et al. In vitro study on silk fibroin textile structure for anterior cruciate ligament regeneration. *Mater Sci Eng C Mater Biol Appl* 2013;33(7):3601–8.
- [59] Bertoldi S, Farè S, Haugen HJ, Tanzi MC. Exploiting novel sterilization techniques for porous polyurethane scaffolds. *J Mater Sci Mater Med* 2015;26(5):182.
- [60] Tiainen H, Lyngstadaas SP, Ellingsen JE, Haugen HJ. Ultra-porous titanium oxide scaffold with high compressive strength. *J Mater Sci Mater Med* 2010;21(10):2783–92.
- [61] Ruggiu A, Tortelli F, Komlev VS, Peyrin F, Cancedda R. Extracellular matrix deposition and scaffold biodegradation in an in vitro three-dimensional model of bone by X-ray computed microtomography. *J Tissue Eng Regen Med* 2014;8(7):557–65.
- [62] Almela T, Brook IM, Moharamzadeh K. Development of three-dimensional tissue engineered bone-oral mucosal composite models. *J Mater Sci Mater Med* 2016;27(4):65.
- [63] Park HJ, Min KD, Lee MC, Kim SH, Lee OJ, Ju HW, et al. Fabrication of 3D porous SF/ β -TCP hybrid scaffolds for bone tissue reconstruction. *J Biomed Mater Res A* 2016; 104(7):1779–87.
- [64] Polak SJ, Candido S, Levengood SK, Johnson AJ. Automated segmentation of micro-CT images of bone formation in calcium phosphate scaffolds. *Comput Med Imaging Graph* 2012;36(1):54–65.
- [65] Palmer AW, Guldberg RE, Levenston ME. Analysis of cartilage matrix fixed charge density and three-dimensional morphology via contrast-enhanced microcomputed tomography. *Proc Natl Acad Sci U S A* 2006;103(51):19255–60.
- [66] McFadden TM, Duffy GP, Allen AB, Stevens HY, Schwarzmaier SM, Plesnila N, et al. The delayed addition of human mesenchymal stem cells to pre-formed endothelial cell networks results in functional vascularization of a collagen-glycosaminoglycan scaffold in vivo. *Acta Biomater* 2013;9(12):9303–16.
- [67] Bi L, Jung S, Day D, Neidig K, Dusevich V, Eick D, et al. Evaluation of bone regeneration, angiogenesis, and hydroxyapatite conversion in critical-sized rat calvarial defects implanted with bioactive glass scaffolds. *J Biomed Mater Res A* 2012;100(12):3267–75.
- [68] Zou D, Zhang Z, He J, Zhang K, Ye D, Han W, et al. Blood vessel formation in the tissue-engineered bone with the constitutively active form of HIF-1 α mediated BMSCs. *Biomaterials* 2012;33(7):2097–108.
- [69] Schmidt C, Bezuidenhout D, Beck M, Van der Merwe E, Zilla P, Davies N. Rapid three-dimensional quantification of VEGF-induced scaffold neovascularisation by micro-computed tomography. *Biomaterials* 2009;30(30):5959–68.
- [70] Young S, Kretlow JD, Nguyen C, Bashoura AG, Baggett LS, Jansen JA, et al. Micro-computed tomography characterization of neovascularization in bone tissue engineering applications. *Tissue Eng B Rev* 2008;14(3):295–306.
- [71] Bolland BJ, Kanczler JM, Dunlop DG, Oreffo RO. Development of in vivo μ CT evaluation of neovascularisation in tissue engineered bone constructs. *Bone* 2008;43(1): 195–202.
- [72] Guldberg RE, Ballock RT, Boyan BD, et al. Analyzing bone, blood vessels, and biomaterials with microcomputed tomography. *IEEE Eng Med Biol Mag* 2003;22(5): 77–83.
- [73] Yin G-C, Tang M-T, Song Y-F, Chen F-R, Liang KS, Duewer FW, et al. Energy-tunable transmission X-ray microscope for differential contrast imaging with near 60 nm resolution tomography. *Appl Phys Lett* 2006;88:241115.

- [74] Papadimitropoulos A, Friess S, Beckmann F, Salmon P, Riboldi S, Hutmacher D, et al. Comparative study of desktop- and synchrotron radiation-based micro computed tomography analyzing cell-seeded scaffolds in tissue engineering of bone. In: Stock SR, editor. *Developments in X-ray tomography VI*, vol. 7078. San Diego, CA, USA: SPIE Proceedings; 2008. <http://dx.doi.org/10.1117/12.797427>.
- [75] Attwood D. Microscopy: nanotomography comes of age. *Nature* 2006;442:642–3.
- [76] Ogurreck M, Wilde F, Herzen J, Beckmann F, Nazmov V, Mohr J, et al. The nanotomography endstation at the PETRA III Imaging Beamline. *J Phys Conf Ser* 2013;425:182002.
- [77] Heim S, Guttman P, Rehbein S, Werner S, Schneider G. Energy-tunable full-field x-ray microscopy: cryo-tomography and nano-spectroscopy with the new BESSY TXM. *J Phys Conf Ser* 2009;186:012041.
- [78] Langer M, Pacureanu A, Suhonen H, Grimal Q, Cloetens P, Peyrin F. X-ray phase nanotomography resolves the 3D human bone ultrastructure. *PLoS One* 2012;7(8): e35691.
- [79] Vatsa A, Breuls RG, Semeins CM, Salmon PL, Smit TH, Klein-Nulend J. Osteocyte morphology in fibula and calvaria—is there a role for mechanosensing? *Bone* 2008; 43(3):452–8.
- [80] Salmon PL, Sasow AY. Application of nano-CT and high-resolution micro-CT to study bone quality and ultrastructure, scaffold biomaterials and vascular networks. *Advanced bioimaging technologies in assessment of the quality of bone and scaffold materials*. Springer; 2007. 323–331.
- [81] Karageorgiou V, Kaplan D. Porosity of 3D biomaterial scaffolds and osteogenesis. *Biomaterials* 2005;26(27):5474–91.
- [82] Morris DE, Mather ML, Simon Jr. CG, Crowe JA. Time-optimized X-ray micro-CT imaging of polymer based scaffolds. *J Biomed Mater Res B Appl Biomater* 2012; 100B(2):360–7.
- [83] Duvall CL, Taylor WR, Weiss D, Guldberg RE. Quantitative microcomputed tomography analysis of collateral vessel development after ischemic injury. *Am J Physiol-Heart Circ Physiol* 2004;287(1):H302–10.
- [84] Mayo SC, Stevenson AW, Wilkins SW. In-line phase-contrast X-ray imaging and tomography for materials science. *Materials* 2012;5(5):937–65.
- [85] Djukic LP, Herszberg I, Walsh WR, Schoepner GA, Prusty BG, Kelly DW. Contrast enhancement in visualisation of woven composite tow architecture using a MicroCT Scanner. Part 1: fabric coating and resin additives. *Compos A: Appl Sci Manuf* 2009; 40(5):553–65.
- [86] Manickam S, McCutcheon JR. Characterization of polymeric nonwovens using porosimetry, porometry and X-ray computed tomography. *J Membr Sci* 2012;407–408: 108–15.
- [87] Vlierberghe SV, Cnudde V, Dubrue P, Masschaele B, Cosijns A, Paeppe ID, et al. Porous gelatin hydrogels: 1. Cryogenic Format Struct Anal Biomacromol 2007;8(2):331–7.